ARTICLE

Fe Nanoparticles Encapsulated in N-doped Porous Carbon for Efficient Oxygen Reduction in Alkaline Media

Chun-Yan Li, Rui Zhang, Xiao-Jie Ba, Xiao-Le Jiang*, Yao-Yue Yang*

Key Laboratory of General Chemistry of the National Ethnic Affairs Commission, School of Chemistry and Environment, Southwest Minzu University, Chengdu, Sichuan, 610041, China

Abstract

Rational design and synthesis of non-precious-metal catalyst plays an important role in improving the activity and stability for oxygen reduction reaction (ORR) but remains a major challenge. In this work, we used a facile approach to synthesize iron nanoparticles encapsulated in nitrogen-doped porous carbon materials (Fe@N-C) from functionalized metal-organic frameworks (MOFs, MET-6). Embedding Fe nanoparticles into the carbon skeleton increases the graphitization degree and the proportion of graphitic N as well as promotes the formation of mesopores in the catalyst. The Fe@N-C-30 catalyst showed the excellent ORR activity in alkaline solutions (E_0 = 0.97 V *vs*. RHE, $E_{1/2}$ = 0.89 V vs. RHE). Moreover, the Fe@N-C-30 catalyst exhibited better methanol resistance and long-term stability when compared to commercial Pt/C. The superior ORR performance could be attributed to the combination of high electrochemical surface area, relative high portion of graphitic-N, unique porous structures and the synergistic effect between the encapsulated Fe particles and the N-doped carbon layer. This work provides a promising method to construct efficient non-precious-metal ORR catalyst through MOFs.

Keywords: Metal-organic frameworks; Porous structures; Fe nanoparticles; Oxygen reduction reaction

1. Introduction

Fuel cells and metal-air batteries have been considered as alternatives to traditional fossil fuels, due to their high energy density, high conversion efficiency and environmentally friendliness [1,2]. However, the efficiency of these energy devices is hampered by the slow kinetics of the cathodic oxygen reduction reaction (ORR) [3]. The most effective ORR catalysts to date are Pt-based ones [4,5], but their limited availability, high price, and poor stability have severely restricted their use on a large-scale [6−8]. Thus, it is urgent and crucial to develop alternative non-noble metal ORR electrocatalysts that are more affordable, efficient and stable.

Recently, carbon-based materials have attracted much attention owing to their tunable structures, earth abundance, and high catalytic activity toward ORR [9−11]. Doping heteroatoms (i.e., N, P, S, B) into the carbon skeletons can induce charge redistribution, enhance the number of active sites and thus improve the ORR performance of carbon materials [12−15]. However, the ORR performance of most heteroatom-doped carbon materials is still less effective compared to commercial Pt/C catalysts [16,17]. Transition metal nanoparticles (TMNPs, usually being Ni, Fe and Co nanoparticles) embedded in N-doped carbon materials (M@N-C) are regarded as a promising approach to further enhance their ORR catalytic activity [18−21], because the TMNPs-embedding treatment could increase catalytic active sites and the graphitic degree of the carbon materials [22,23]. Meanwhile, electronic interactions between N-doped carbon layers and transition metals can further improve the ORR catalytic performance.

Received 24 October 2022; Received in revised form 2 December 2022; Accepted 14 December 2022
Available online 16 December 2022

* Corresponding author, Yao-Yue Yang, Tel: (86-28)85709707, E-mail address: yaoyueyoung@swun.edu.cn.
* Corresponding author, Xiao-Le Jiang, Tel: (86-28)85709707, E-mail address: jiangxl@swun.edu.cn.

https://doi.org/10.13208/j.electrochem.2210241
1006-3471/© 2023 Xiamen University and Chinese Chemical Society. This is an open access article under the CC BY-NC license (http://creativecommons.org/licenses/by-nc/4.0/).

For example, Deng et al. [24] synthesized pod-like carbon nanotubes encapsulated Fe nanoparticles for ORR. The catalysts exhibited high catalytic activity and long-term durability in proton exchange membrane fuel cells (PEMFC). According to DFT calculations, electron transferred from Fe particles to the CNTs, which decreased the local work function on the carbon surface, could be the sources of the enhanced catalytic activity. Recently, Zhang et al. [25] synthesized N-doped carbon nanotube-encapsulated cobalt nanoparticles (Co@NCNTs) using silica colloids and triblock copolymers as hard and soft templates, respectively. The Co@NCNTs-800 catalyst showed higher ORR performance as well as better methanol tolerance and durability, compared with commercial Pt/C. The excellent catalytic activity toward ORR originated from the combination of nitrogen doping, unique structure, large surface area and the synergistic effect between cobalt nanoparticles and N-doped carbon layers. Despite these advances, most of the preparation processes are time-consuming and difficult to remove the templates. Meanwhile, it remains a great challenge to further enhance the ORR performance of carbon-based catalysts. Therefore, developing a simple and straightforward method to synthesize transition metal and N co-doped carbon materials with enhanced ORR catalytic activity is still necessary and urgent.

Fortunately, metal-organic frameworks (MOFs) have been regarded as promising precursors to prepare carbon-based nanomaterials, due to the advantages of high surface area, tunable porosity and structures as well as easy functionalization [22,26]. In addition of self-sacrificing templates, MOFs are also acted as carbon and nitrogen sources. Usually, MOFs-derived carbon-based materials feature large specific surface area, porous structures and abundant catalytic active sites, which would facilitate the mass transfer of reactants and products, and exhibit high ORR performance [27,28].

In this work, we developed a facile approach to synthesize Fe nanoparticles encapsulated in N-doped porous carbon materials (Fe@N-C) from functionalized MOFs (MET-6). The functionalized MET-6 was achieved by simple impregnation with ammonium ferric citrate (AFC). The Fe@N-C catalysts were obtained after high-temperature pyrolysis and acid leaching. The Fe@N-C-30 catalyst showed the excellent ORR activity in alkaline solutions with the onset reduction potential (E_0) and the half-wave potential ($E_{1/2}$) being 0.97 and 0.89 V vs. RHE, respectively. Moreover, the Fe@N-C-30 catalyst exhibited better methanol resistance and stability compared with commercial Pt/C.

2. Experimental section

2.1. Chemicals

Zinc chloride ($ZnCl_2$, >98%), 1H-1, 2, 3-triazole (≥98.0%), aqueous ammonia (25%−28%), N, N-dimethylformamide (DMF, 99.5%), ethanol(C_2H_5OH, ≥99.7%), potassium hydroxide (KOH, ≥99.0%), perchloric acid ($HClO_4$,70%−72%) were all purchased from Shanghai McLean Biochemical Technology Co., Ltd. Ammonium ferric citrate ($C_6H_{11}FeNO_7$, AFC) was purchased from J&K Scientific Ltd. All chemicals and solvents were used without further purification.

2.2. Preparation of catalysts

The synthesis process of Fe@N-C catalysts is illustrated in Scheme 1. Firstly, the MET-6 was prepared by a simple method reported in the previous work [29]. Then MET-6 was functionalized with AFC by a simple impregnation method. Subsequently, the precursor was annealed at 900 °C in Ar atmosphere. Finally, Fe nanoparticles encapsulated in N-doped porous carbon materials (Fe@N-C) were obtained after acid-leaching. The details are described in the following sections.

Synthesis of MET-6

5.0 g $ZnCl_2$ was dissolved in the mixture of 50 mL ethanol, 20 mL aqueous ammonia, 75 mL deionized water and 50 mL DMF. Then 6.26 mL of 1H-1, 2, 3-triazole was added into the solution and stirred for 24 h at room temperature. Finally, the MET-6 was obtained after centrifugation and dried under vacuum.

Synthesis of Fe@N-C-30 catalyst

30 mg of AFC was dissolved in 60 mL deionized water, and then 1.0 g MET-6 was added into the above solution. After string for 25 h, the functionalized MET-6 (AFC/MET-6-30) was collected after being filtered and dried at 70 °C. Subsequently, the AFC/MET-6-30 precursor was pyrolyzed at 900 °C for 3 h in Ar atmosphere. The resulted black power was acid-washed with 0.5 $mol \cdot L^{-1}$ $HClO_4$ for 16 h. After filtering and drying at 60 °C overnight, the products were obtained and are named as Fe@N-C-30. For comparison, N-C and Fe@N-C-60 were synthesized by the similar process, except that different amounts of AFC (0 and 60 mg) were added during the impregnation process.

2.3. Characterizations

The X-Ray diffraction (XRD) patterns were recorded on an Ultima IV X-ray diffractometer with Cu K_α radiation. X-ray photoelectron

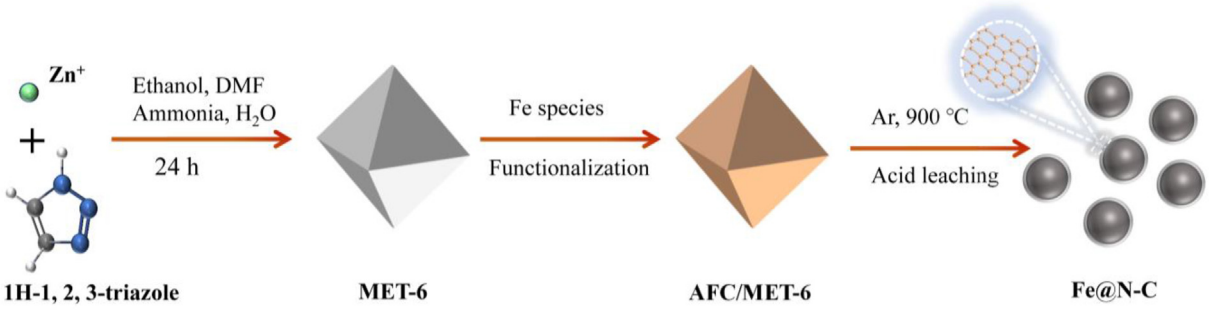

Scheme 1. Schematic illustration showing the preparation process of Fe@N-C catalysts.

spectroscopic (XPS) spectra were measured by Thermo SCIENTIFIC ESCALAB 25Xi spectrometer. Transmission electron microscopic (TEM) images were obtained using a Japan-JEOL-JEM 2100 F transmission electron microscope. N_2 adsorption/desorption isotherms were collected by Quantachrome Autosorb-iQ2 system. The specific surface areas and pore distributions were evaluated by Brunauer-Emmett-Teller (BET) and density functional theory (DFT) methods. Raman spectrum measurements were carried out on a Japan-HORIBA-XploRA Plus with a radiation of 532 nm from a liquid nitrogen-cooled He-Ne laser.

2.4. Electrochemical measurements

Rotating disk electrode (RDE) measurements were performed by MSR Electrode Rotator from Pine Research Instrument, while the potential control and current collection were generally performed on a three-electrode system by a CHI660E electrochemical workstation (Shanghai CH Instruments). The Hg/HgO electrode and carbon rod electrode were applied as the reference electrode and the counter electrode, respectively. To prepare the working electrode, 5.0 mg catalyst was mixed with 50 μL Nafion solution (5 wt%) and 2 mL ethanol, and followed by ultrasonication for 30 min to form homogenous catalyst ink. Then, 25 μL of the catalyst ink was dropped onto a cleaned glassy carbon (GC) disk electrode (5 mm in diameter) and dried at room temperature. Before the electrochemical tests, the electrolyte (0.1 $mol \cdot L^{-1}$ KOH) was bubbled with high-purity O_2 at least 30 min. The linear sweep voltammetric (LSV) measurements were carried out using RDE with various rotating speeds from 400 to 2500 rpm at a scan rate of 10 $mV \cdot s^{-1}$. The methanol tolerance test was performed by adding anhydrous methanol into O_2-saturated 0.1 $mol \cdot L^{-1}$ KOH solution at the time of 500 s. For comparison, 40 wt% Pt/C (25 $\mu g \cdot cm^{-2}$) was coated on the GC and RDE electrodes to carry out the similar electrochemical tests.

The electron transfer number (n) during ORR was estimated by the following Kouteckye-Levich (K-L) equations:

$$\frac{1}{J}=\frac{1}{J_L}+\frac{1}{J_K}=\frac{1}{B\omega^{\frac{1}{2}}}+\frac{1}{J_K} \quad (1)$$

$$B=0.62nFC_0D_0^{\frac{2}{3}}v^{-\frac{1}{6}} \quad (2)$$

where J is the measured current density, J_K and J_L are the kinetic current density and diffusion-limited current density, respectively, ω is the angular velocity ($\omega = 2\pi N$, N is the rotation rate), n is the transferred electron number, F is Faraday constant (96,485 $C \cdot mol^{-1}$), C_0 is the concentration of O_2 in the electrolyte (1.2×10^{-6} $mol \cdot cm^{-3}$), D_0 is the diffusion coefficient of O_2 (1.9×10^{-5} $cm^2 \cdot s^{-1}$), and v is the electrolyte kinetic viscosity (0.01 $cm^2 \cdot s^{-1}$) at room temperature.

The double-layer capacitance C_{dl} was used to roughly evaluated the electrochemical active surface area (ECSA), since ECSA is generally proportional to C_{dl}. For ideal capacitors, a steady-state capacitive current (i_C) in a short time is related to the capacitance (C) and to the scan rate (v) as described $i_C = Cv$. To obtain the double-layer capacitance, cyclic voltammograms at various scan rates were recorder within a potential region of 1.07−1.17 V (vs. RHE) with multiple scan rates where no redox processes take place, extracting i_C from the anodic and cathodic scans of the recorded voltammograms, and subsequently extracting C_{dl} from the slope of the resulting i_C vs C_{dl} plot [30].

All the measured potential converted to the RHE values using the formula: $E_{RHE} = E_{Hg/HgO} + 0.0592\ pH + 0.098$, where 0.098 is the potential difference between the Hg/HgO (1 $mol \cdot L^{-1}$ NaOH) and the standard hydrogen electrode (SHE), E_{RHE} and $E_{Hg/HgO}$ are the potential values versus the reference electrode of RHE and Hg/HgO, respectively.

3. Results and discussion

3.1. Morphological and structural characteristics

The XRD patterns of all the catalysts are shown in Fig. 1A. For the Fe@N-C-30 and Fe@N-C-60, the characteristic diffraction peaks at 43.6°, 50.8°and 74.8° are attributed to (111), (200) and (220) crystal planes of Fe (ICDD-PDF #01-081-775) [31]. No peaks related to the metallic Fe are observed in the pattern of N-C. The two broad diffraction peaks at 26° and 44° are belonged to the (002) and (100) planes of graphitic carbon [32]. Raman spectra were measured to assess the graphitization degrees. As shown in Fig. 1B, all catalysts exhibit two Raman bands at 1340 and 1590 cm^{-1}, which are assigned to defective band (D) and graphitic band (G) of carbon, respectively [33]. The intensity ratio of D and G bands (I_D/I_G) of N−C is higher than those of Fe@N-C-30 and Fe@N-C-60, implying that the graphitization degree is increased by the doping of Fe. This could improve the electrical conductivity of the catalyst and thus facilitate charge transfer in the electrochemical reaction [34].

The structures and morphologies of the catalysts were characterized by TEM. As shown in Fig. 2A, the N−C catalyst shows a porous structure. The TEM images of Fe@N-C-30 and Fe@N-C-60 indicate that the Fe nanoparticles were embedded in porous carbon (Fig. 2B and C). The HRTEM image of Fe@N-C-30 is displayed in Fig. 2D. The lattice fringes of 0.206 nm and 0.33 nm are corresponding to the (111) plane of Fe and (002) plane of graphitic carbon, which are consistent with the XRD results. The above results clearly reveal that the Fe nanoparticles are encapsulated in N-doped porous carbon.

The specific surface area and pore structure of the catalysts were analyzed by N_2 adsorption/desorption isotherms. As shown in Fig. 3A, all the samples show an obvious hysteresis loop in a wide relative pressure (P/P_0) range, indicative of the existence of mesopores, which is consistent with the TEM results. The hysteresis loops of Fe@N-C-30 and Fe@N-C-60 are bigger than that of N−C, implying higher contents of mesopores in Fe@N-C-30 and Fe@N-C-60 than that in N-C. Fig. 3B shows the pore size distribution plots of N-C, Fe@N-C-30 and Fe@N-C-60, revealing that the mesopores with sizes of 2.8−5 nm are produced in the samples. In addition, the BET surface areas of N-C, Fe@N-C-30 and Fe@N-C-60 are 357.2, 861.4 and 742.3 $m^2 \cdot g^{-1}$, respectively (Table 1). The external surface areas of Fe@N-C-30 and Fe@N-C-60 are much larger than that of N-C, indicating that the Fe doping has positive effect on the formation of mesopores. Large amounts of mesopores, and the high BET surface areas of Fe@N-C-30 and Fe@N-C-60 catalysts would expose much active sites, facilitate the mass transport and further enhance the ORR performance [25,33].

X-ray photoelectron spectroscopy (XPS) was employed to investigate surface compositions and chemical states of Fe@N-C-30 and Fe@N-C-60 catalysts. The survey XPS spectra in Fig. 4A show that C, N, O, and Fe elements are presented in the catalyst. Fig. 4B shows the high-resolution N 1s spectra of Fe@N-C-30 and Fe@N-C-60 catalysts. The N 1s spectra are deconvoluted into four types of nitrogen species, including pyridinic N (398.4 ± 0.2 eV), pyrrolic N (400 ± 0.2 eV), graphitic N (401 ± 0.2 eV) and oxidized N (>404.0 eV) [35,36]. As shown in Table 2, the percentage of graphitic N increases after Fe doping, and Fe@N-C-30 has the largest value, which would improve the ORR performance [37,38]. The high resolution XPS spectra of Fe 2p in Fig. 4C show three pairs of peaks. The signals at 707.6 and 718.6 eV are assigned to Fe^0. And the signals at 710.3, 723. eV, 714.5 and 726.5 eV are belonged to oxidized Fe species, due to the surface oxidation of Fe nanoparticles when exposed to air [39,40]. Notably, the peak at 710.25 eV of Fe@N-C-30 shows a left shift by

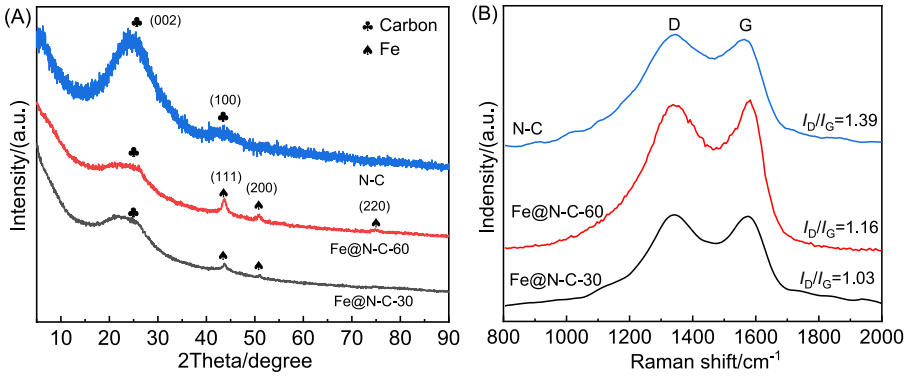

Fig. 1. (A) XRD patterns and (B) Raman spectra of different catalysts.

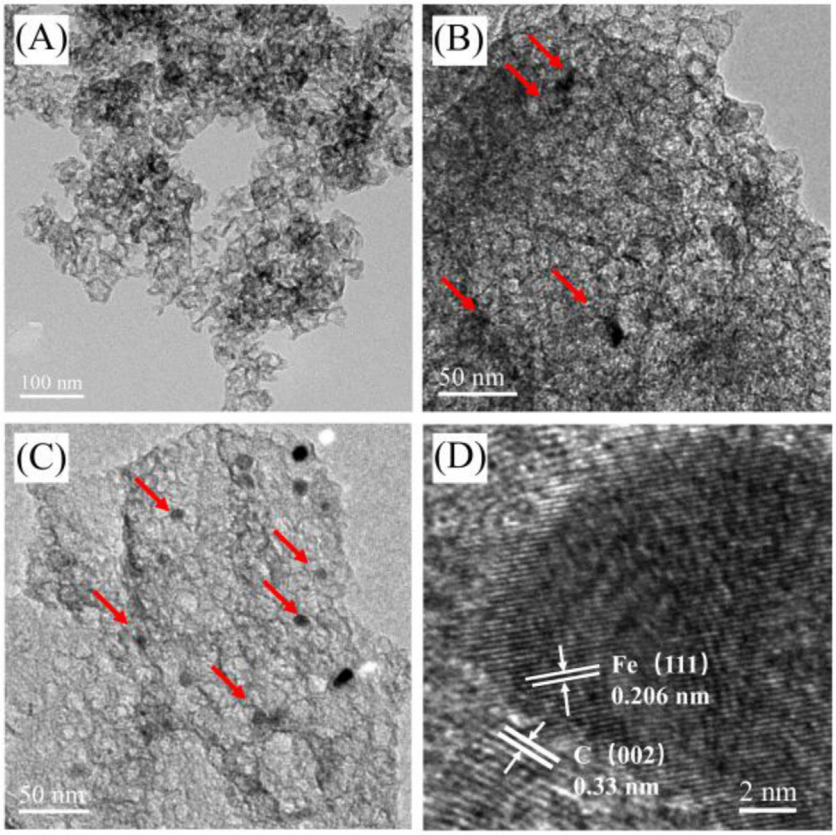

Fig. 2. TEM images of (A) N-C, (B) Fe@N-C-30 and (C) Fe@N-C-60 (Red arrows in B-C indicate to the Fe nanoparticles), and (D) HRTEM image of Fe@N-C-30.

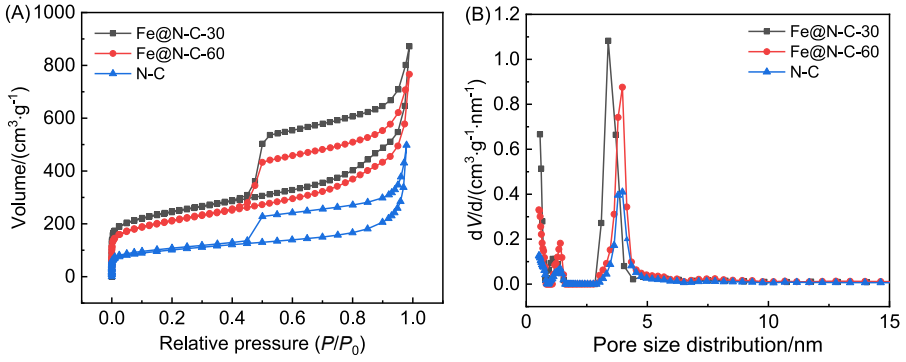

Fig. 3. (A) N_2 adsorption/desorption isotherms and the pore size distribution plots (B) for N-C, Fe@N-C-30 and Fe@N-C-60.

0.66 eV compared to Fe@N-C-60 (709.59 eV), which may be caused by the stronger interactions between Fe particles and the N-doped carbon layer [41].

3.2. Electrochemical performance evaluation

The electrocatalytic performance toward ORR of different catalysts was assessed by LSV

Table 1. The information of BET surface area and porosity characters of different catalysts.

Sample	Surface area ($m^2 \cdot g^{-1}$)	Micropore area ($m^2 \cdot g^{-1}$)	External surface area ($m^2 \cdot g^{-1}$)	V_{total} ($cm^3 \cdot g^{-1}$)	V_u ($cm^3 \cdot g^{-1}$)	ΔV ($cm^3 \cdot g^{-1}$)
Fe@N-C-30	861.4	410.4 42	450.936	1.349	0.185	1.164
Fe@N-C-60	742.3	279.085	463.248	1.185	0.125	1.060
N-C	357.2	198.504	158.665	0.77	0.098	0.672

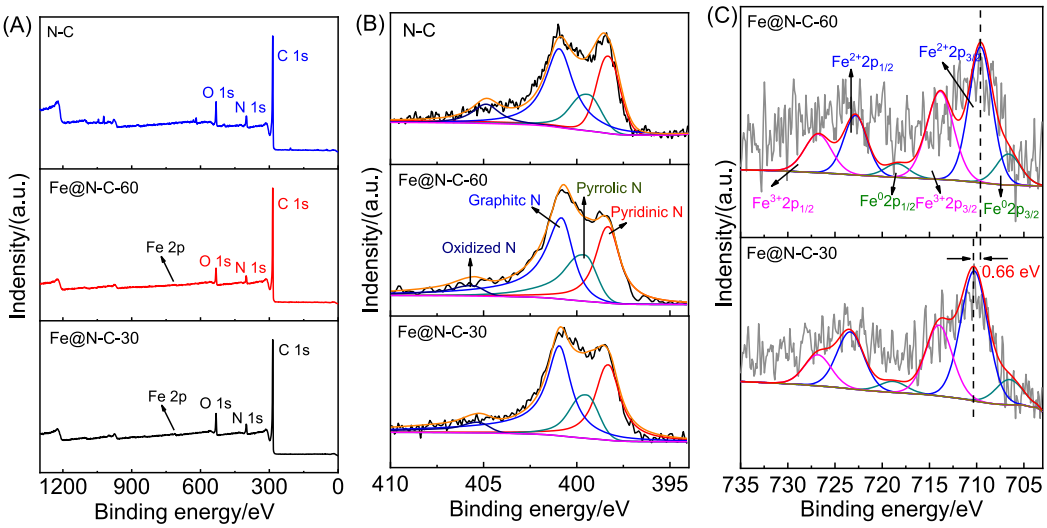

Fig. 4. (A) Survey XPS spectra, and high-resolution (B) N 1s and (C) Fe 2p XPS spectra of Fe@N-C-30 and Fe@N-C-60 catalysts.

Table 2. The element content analyzed by XPS.

Sample	Total nitrogen content (wt%)	Percentage of nitrogen species (%)			
		pyridinic	pyrrolic	graphitic	oxidized
N-C	8.15	33.36	22.80	36.85	7
Fe@N-C-30	7.29	31.52	16.29	45.8	6.4
Fe@N-C-60	6.14	31.64	22.30	40.14	5.92

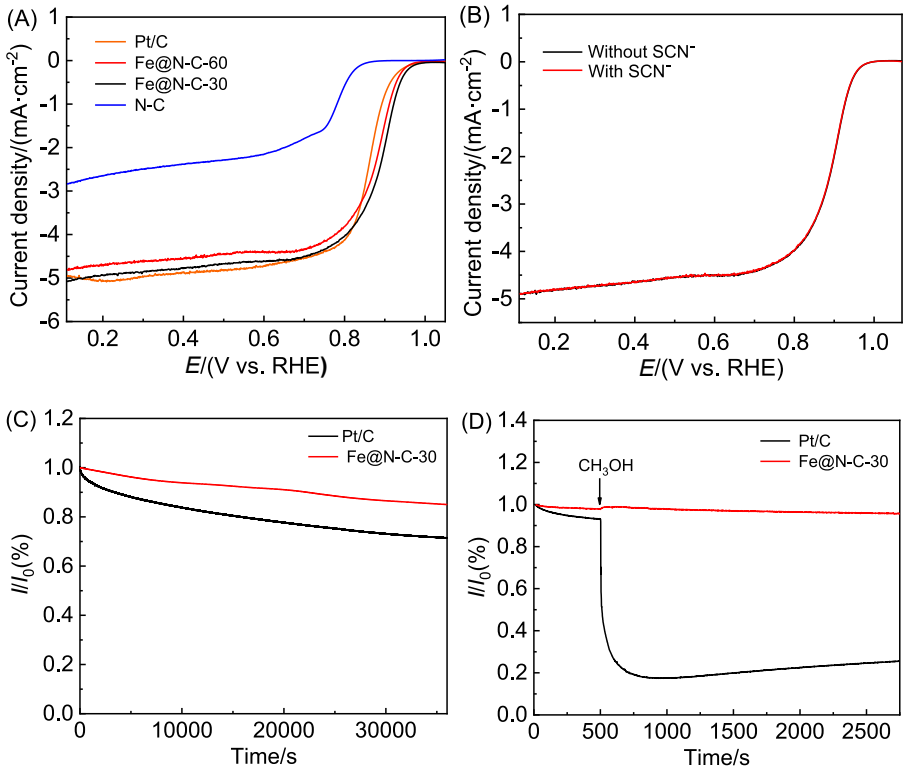

Fig. 5. (A) LSV curves of different samples in O_2 saturated 0.1 mol·L^{-1} KOH, (B) SCN^- poisoning test of Fe@N-C-30 measured in O_2-saturated KOH, (C) Long-term stability test and (D) methanol tolerance test for Fe@N-C-30 and Pt/C.

measurements in an alkaline electrolyte [42]. LSV curves of N-C, Fe@N-C-30 and Fe@N-C-60, and commercial 40 wt% Pt/C for ORR with 1600 rpm in O_2-saturated 0.1 mol·L^{-1} KOH are shown in Fig. 5. The onset potential (E_o) of Fe@N-C-30 is 0.97 V (vs. RHE), which shifts 20 mV positively compared to those of Fe@N-C-60 and commercial Pt/C. And the half-wave potentials ($E_{1/2}$) of Fe@N-C-30 and Fe@N-C-60 are 0.89 V and 0.88 V (vs. RHE), respectively, which are more positive than that of commercial Pt/C (0.86 V), indicating the enhanced ORR performance. Generally, the ORR catalytic activity of Fe@N-C-30 catalyst is comparable to those reported for carbon-encapsulated metals or metal-nitrogen-carbon catalysts (Table 3). Apparently, the E_o and $E_{1/2}$ of Fe@N-C-30 and Fe@N-C-60 are much more positive than that of N-C, so do the limiting current densities. The inferior ORR activity of N-C can be mainly attributed to the absence of Fe species, confirming that the encapsulated Fe nanoparticles play an important role in promoting the ORR. In addition, to exclude the possible surface Fe-N_x sites as active sites for ORR, the SCN^- poison test was performed in O_2-

Table 3. Summary of the recently reported carbon-encapsulated metals and/or M-N-C catalysts for ORR in alkaline media.

Catalyst	Catalyst loading (mg·cm^{-2})	E_{onset} (V vs. RHE)	$E_{1/2}$ (V vs. RHE)	Reference
Fe@N-C-30	0.3	0.97	0.89	This work
Fe@N-C NT/NSs	0.16	0.86	0.75	[43]
Co@C@TiO_2	0.25	0.867	0.68	[18]
Co@NCNTs-800	0.3	0.88	0.75	[25]
Fe-N-C Act	0.2	/	0.9	[44]
Fe-N-C	0.23	0.95	0.85	[45]
Co@N-C(DM)	1.4	0.90	0.83	[22]
Co/N-CNN	0.76	/	0.865	[19]
Co-N-pCNs	0.25	0.96	0.8	[46]
Fe-N/P-C-700	0.6	0.941	0.867	[47]
3DOM Fe-N-C	0.61	/	0.875	[48]
Fe©N-C−12	0.31	0.95	0.83	[49]
FeSA-N-C	0.28	1	0.89	[50]
Fe-CZIF-800-10	0.22	0.982	0.830	[51]
Fe@C_2N	0.7	1.015	0.876	[52]
Fe-N-C(Fe-AC)	/	/	0.915	[53]

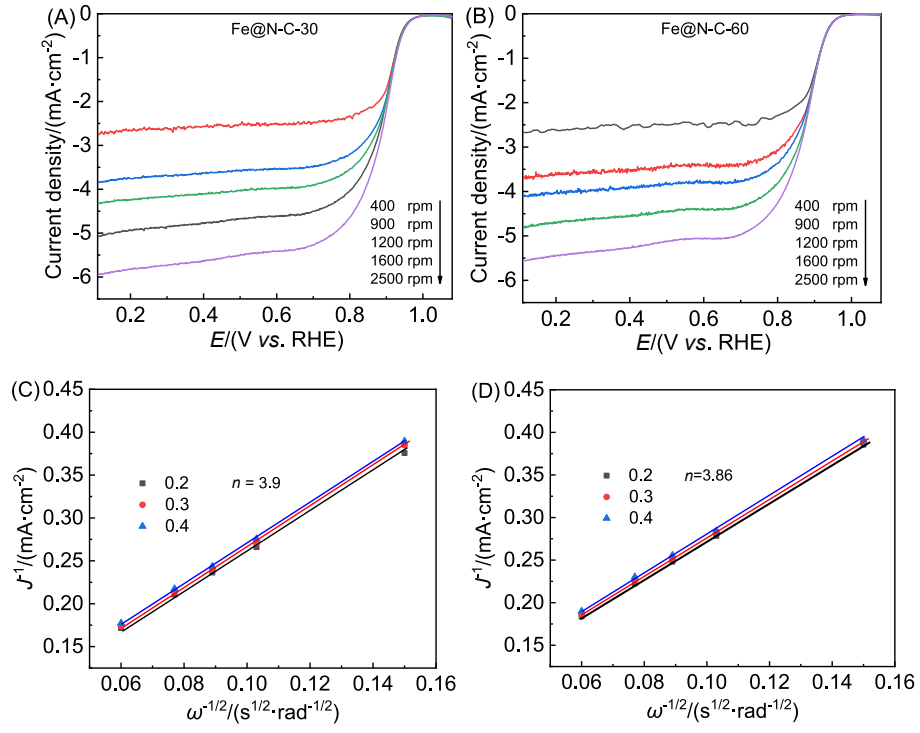

Fig. 6. RDE curves of different catalysts for ORR at different rotating speeds with scan rate of 10 mV·s^{-1} in O_2-saturated 0.10 mol·L^{-1} KOH (A,B), and the corresponding K-L plots (C,D).

saturated 0.1 mol·L^{-1} KOH. As shown in Fig. 5B, Fe@N-C-30 exhibits almost the same ORR catalytic activity with and without SCN^- adsorption, implying no deterioration of the ORR activity. These results reveal that no surface exposed Fe species (i.e., Fe-N_x sites) are active for ORR and the Fe nanoparticles coated by N-doped carbon may be the predominant factor for promoting the ORR electrocatalytic performance of Fe@N-C-30 [54].

The durability and methanol-tolerance are important requirements for the practical applications of the ORR catalysts [27,55]. Fig. 5C shows the stability evaluation of Fe@N-C-30 and commercial Pt/C. Under the potential of 0.8 V (vs. RHE), Fe@N-C-30 retained 85% of the initial current density after 36,000 s, much better than that of the Pt/C (71% retained). The chronoamperometric responses of the Fe@N-C-30 and Pt/C were tested in the O_2-saturated 0.1 mol·L^{-1} KOH after adding methanol at 500 s. As shown in Fig. 5D, no obvious decrease of the current over Fe@N-C-30 is observed, while the current of commercial Pt/C decreases significantly because of the methanol oxidation. All these results suggest that Fe@N-C-30 is a promising ORR catalyst with good long-time durability and methanol tolerance.

To elucidate the ORR mechanism on different catalysts, RDE curves recorded at different rotation speeds are depicted in Fig. 6A,B. The Koutecky-Levich plots (Fig. 6C,D) at various potentials exhibit good first-order reaction kinetics related to the concentration of dissolved O_2. According to the K-L equation, the electron transfer numbers (n) are calculated to be about 3.86 and 3.9, and are very close to 4.0, manifesting that the 4-electron pathway occurred on the Fe@N-C-30 and Fe@N-C-

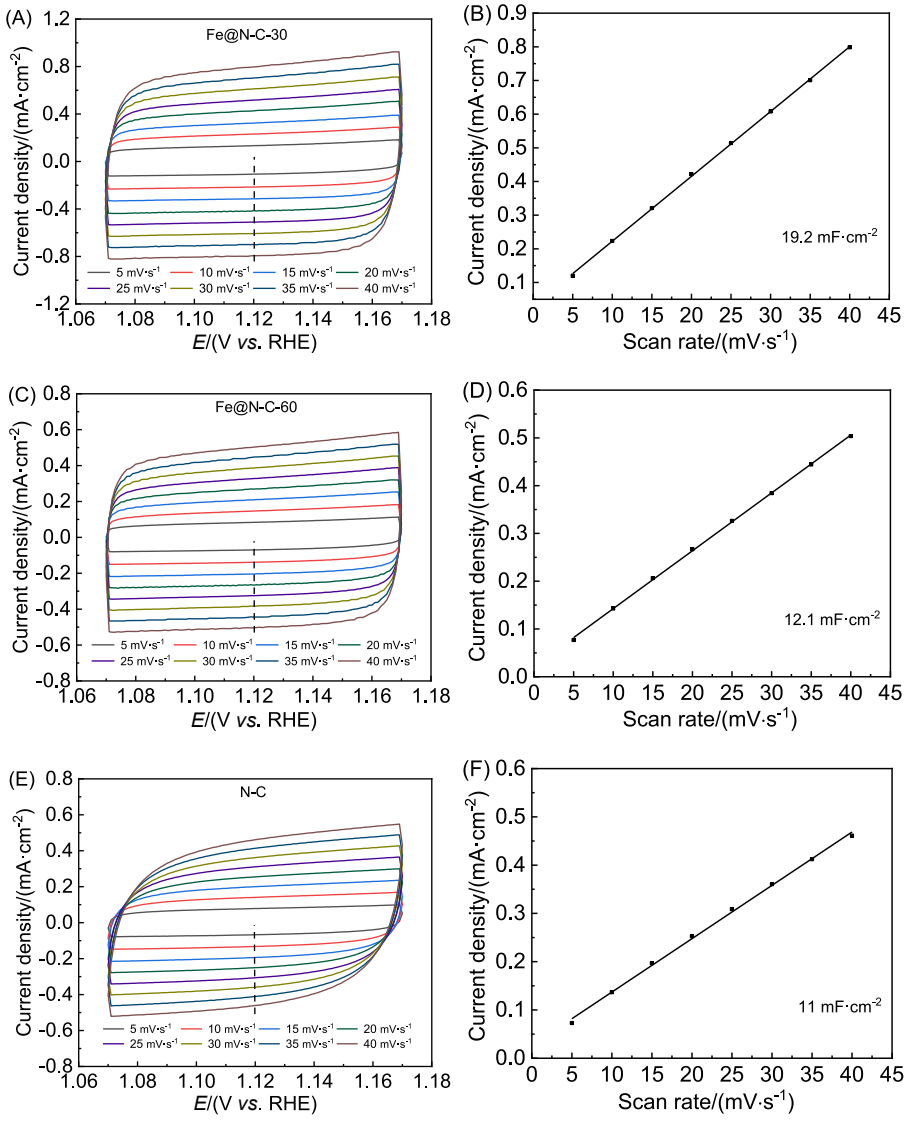

Fig. 7. ECSA measurements of (A,B) Fe@N-C-30, (C,D) Fe@N-C-60 and (E-F) N-C.

60 catalysts, which is consistent with the superior electrocatalytic activity [56,57].

In addition, the ECSA represents the actual amount of electrochemical active sites exposed in the catalyst. We estimated ECSAs of the catalysts by measuring the C_{dl}, which is calculated by the slope of the linear fitting curve. As shown in Fig. 7, the C_{dl} value of Fe@N-C-30 (19.2 $mF \cdot cm^{-2}$) is much higher than those of Fe@N-C-60 (12.1 $mF \cdot cm^{-2}$), and N-C (11 $mF \cdot cm^{-2}$), which is coincidence with the BET results, indicating that the mesoporous structure could offer more exposed active sites and further enhance the ORR performance [58].

Therefore, the excellent ORR performance of Fe@N-C-30 could be attributed to the following reasons: (1) the doping of Fe increased the graphitization degree of carbon layer and proportion of graphitic N, as well as promotes the formation of mesopores, which could expose a large number of electrochemical active sites, facilitate charge transfer/mass transport and thus enhance the ORR activity [25,33]. (2) previous works on transition metal nanoparticles encapsulated in carbon shell for ORR have proposed that the electron transfer from the encapsulated metal nanoparticles to the contact carbon shells could increase the charge density of carbon layers, which would facilitate the activation of O_2 and furtherly enhance the ORR kinetics [24,43,59−61]. Therefore, the synergetic interaction of Fe nanoparticles with the N-doped carbon layer may play important role in enhancing the ORR electrocatalytic activity.

4. Conclusions

In summary, we proposed a facile approach to synthesize Fe nanoparticles encapsulated in N-doped porous carbon materials (Fe@N-C) from functionalized MOFs. The Fe@N-C-30 catalyst showed excellent ORR activity in alkaline solutions (E_0 = 0.97 V vs. RHE, $E_{1/2}$ = 0.89 V vs. RHE). Moreover, the Fe@N-C-30 catalyst exhibited better methanol resistance and long-term stability compared with commercial Pt/C. The excellent ORR catalytic activity could be attributed to the combination of the high electrochemical surface area, relatively high portion of graphitic-N, mesoporous structures and the synergistic effect between the encapsulated Fe particles and the N-doped carbon layer. This work provides a promising method to construct efficient non-precious-metal ORR catalysts through MOFs.

Acknowledgements

This work was supported by the National Natural Science Foundation of China (Grants 22002121, 22172121), and the National Undergraduate Training Program for Innovation and Entrepreneurship (Grant S202210656087).

References

[1] Hu J, Zhang C X, Sun M Z, Qi Q L, Luo S X, Song H C, Xiao J Y, Huang B L, Leung M KH, Zhang Y J. Ultrastable bimetallic Fe_2Mo for efficient oxygen reduction reaction in pH-universal applications[J]. Nano Res., 2022, 15(6): 4950−4957.

[2] Liu M M, Zhang R Z, Chen W. Graphene-supported nanoelectrocatalysts for fuel cells: synthesis, properties, and applications[J]. Chem. Rew., 2014, 114(10): 5117−5160.

[3] Xu L Y, Yu M Z, Yang P J, Wang Z Y, Qiu J S. Caging porous Co-N-C nanocomposites in 3D graphene as active and aggregation-resistant electrocatalyst for oxygen reduction reaction[J]. J. Electrochem., 2018, 24(6): 715−725.

[4] Ye L, Chai G L, Wen Z H. Zn-MOF-74 derived N-doped mesoporous carbon as pH-universal electrocatalyst for oxygen reduction reaction[J]. Adv. Funct. Mater., 2017, 27(14): 8.

[5] Zaman S, Huang L, Douka A I, Yang H, You B, Xia B Y. Oxygen reduction electrocatalysts toward practical fuel cells: progress and perspectives[J]. Angew. Chem. Int. Ed., 2021, 60(33): 17832−17852.

[6] Zhang X R, Lyu D D, Mollamahale Y B, Yu F, Qing M, Yin S B, Zhang X Y, Tian Z Q, Shen P K. Critical role of iron carbide nanodots on 3D graphene based nonprecious metal catalysts for enhancing oxygen reduction reaction[J]. Electrochim. Acta, 2018, 281: 502−509.

[7] Liu X, Park M, Kim M G, Gupta S, Wang X J, Wu G, Cho J. High-performance non-spinel cobalt-manganese mixed oxide-based bifunctional electrocatalysts for rechargeable zinc-air batteries[J]. Nano Energy, 2016, 20: 315−325.

[8] Sui S, Wang X Y, Zhou X T, Su Y H, Riffat S, Liu C J. A comprehensive review of Pt electrocatalysts for the oxygen reduction reaction: nanostructure, activity, mechanism and carbon support in PEM fuel cells[J]. J. Mater. Chem. A, 2017, 5(5): 1808−1825.

[9] Li T, Zhao H X, Wang R L, Wang S Y. Carbon-based, metal-free electrocatalysts for renewable energy technologies[J]. Prog. Mater. Sci. 2021;(116): 313−334.

[10] Prati L, Chan-Thaw C E, Campisi S, Villa A. N-modified carbon-based materials: nanoscience for catalysis[J]. Chem. Rec., 2016, 16(5): 2187−2197.

[11] Jaleh B, Nasrollahzadeh M, Eslamipanah M, Nasri A, Shabanlou E, Manwar N R, Zboril R, Fornasiero P, Gawande M B. The role of carbon-based materials for fuel cells performance[J]. Carbon, 2022, 198: 301−352.

[12] Zhang J, Zhang J J, He F, Chen Y J, Zhu J W, Wang D L, Mu S C, Yang H Y. Defect and doping Co-engineered non-metal nanocarbon ORR electrocatalyst[J]. Nanomicro Lett., 2021, 13(1): 65.

[13] Wang Y C, Lai Y J, Song L, Zhou Z Y, Liu J G, Wang Q, Yang X D, Chen C, Shi W, Zheng Y P, Rauf M, Sun S G. S-doping of an Fe/N/C ORR catalyst for polymer electrolyte membrane fuel cells with high power density[J]. Angew. Chem. Int. Ed., 2015, 54(34): 9907−9910.

[14] Jin Z, Nie H, Yang Z, Zhang J, Liu Z, Xu X J, Huang S M. Metal-free selenium doped carbon nanotube/graphene networks as a synergistically improved cathode catalyst for oxygen reduction reaction[J]. Nanoscale, 2012, 4(20): 6455−6460.

[15] Gao J, Wang Y, Wu H, Liu X, Wang L L, Yu Q L, Li A W, Wang H, Song C Q, Gao Z R, Peng M, Zhang M T, Ma N,

Wang J O. Construction of a sp^3/sp^2 carbon interface in 3D N-doped nanocarbons for the oxygen reduction reaction[J]. Angew. Chem. Int. Ed., 2019, 58(42): 15089−15097.
[16] Kim D W, Li O L, Saito N. Enhancement of ORR catalytic activity by multiple heteroatom-doped carbon materials[J]. Phys. Chem. Chem. Phys., 2015, 17(1): 407−413.
[17] Wei P, Li X G, He Z M, Sun X P, Liang Q R, Wang Z Y, Fang C, Li Q, Yang H, Han J T, Huang Y H. Porous N, B co-doped carbon nanotubes as efficient metal-free electrocatalysts for ORR and Zn-air batteries[J]. Chem. Eng. J., 2021, 422: 130134.
[18] He M, Song S J, Wang P, Fang Z, Wang W W, Yuan X L, Li C Y, Li H, Song W Y, Luo D, Li Z X. Carbon doped cobalt nanoparticles stabilized by carbon shell for highly efficient and stable oxygen reduction reaction[J]. Carbon, 2022, 196: 483−492.
[19] Du L, Gao X Y, Li Z, Wang G Y, Wen Z, Yang C C, Jiang Q. Metal-organic frameworks derived Co/N-doped carbon nanonecklaces as high-efficient oxygen reduction reaction electrocatalysts[J]. Int. J. Hydrogen Energy, 2022, 47(92): 39133−39145.
[20] Ni B X, Wu L M, Chen R, Shi C X, Chen T H. Fe/Co-based nanoparticles encapsulated in heteroatom-doped carbon electrocatalysts for oxygen reduction reaction[J]. Sci. China Mater., 2019, 62(11): 1626−1641.
[21] Gao J, Ma N, Zheng Y M, Zhang J F, Gui J Z, Guo C K, An H Q, Tan X Y, Yin Z, Ma D. Cobalt/nitrogen-doped porous carbon nanosheets derived from polymerizable ionic liquids as bifunctional electrocatalyst for oxygen evolution and oxygen reduction reaction[J]. ChemCatChem, 2016, 9(9): 1601−1609.
[22] Wang C X, Yuan H F, Yu F, Zhang J, Li Y Y, Bao W T, Wang Z M, Lu K, Yu J, Bai G, Wang G, Peng B H, Zhang L L. Enhanced oxygen reduction reaction performance of Co@N-C derived from metal-organic frameworks ZIF-67 via a continuous microchannel reactor[J]. Chinese Chem. Lett., 2023, 34(1): 107128.
[23] Sun M, Li Z J, Liu Y Y, Guo D F, Xie Z Y, Huang Q Z. The synthesis of Fe/N-C@ CNFs and its electrochemical performance toward oxygen reduction reaction[J]. Int. J. Hydrogen Energy, 2020, 45(56): 31892−31901.
[24] Deng D H, Yu L, Chen X Q, Wang G X, Jin L, Pan X L, Sun G Q, Bao X H. Iron encapsulated within pod-like carbon nanotubes for oxygen reduction reaction[J]. Angew. Chem. Int. Ed., 2013, 52(1): 389−393.
[25] Liu F, Zhang X Q, Zhang X L, Wang L L, Liu M M, Zhang J J. Dual-template strategy for electrocatalyst of cobalt nanoparticles encapsulated in nitrogen-doped carbon nanotubes for oxygen reduction reaction[J]. J. Colloid Inter. Sci., 2021, 581: 523−532.
[26] Zulys A, Yulia F, Muhadzib N, Nasruddin. Biological metal-organic frameworks (Bio-MOFs) for CO_2 capture[J]. Ind. Eng. Chem. Res., 2020, 60(1): 37−51.
[27] Li S, Feng C, Xie Y H, Guo C Y, Zhang L G, Wang J D. Synthesis of nitrogen-rich porous carbon nanotubes coated Co nanomaterials as efficient ORR electrocatalysts via MOFs as precursor[J]. J. Alloys Compd., 2022, 911: 11.
[28] Xu M J, Liu J, Ge J J, Liu C P, Xing W. Research progress of metal-nitrogen-carbon catalysts toward oxygen reduction reaction inm changchun institute of applied chemistry[J]. J. Electrochem., 2020, 26(4): 464−473.
[29] Tong H G, Wang C L, Lu J, Chen S, Yang K, Huang M X, Yuan Q, Chen Q W. Energetic metal-organic frameworks derived highly nitrogen-doped porous carbon for superior potassium storage[J]. Small, 2020, 16(43): e2002771.
[30] Morales D M, Risch M. Seven steps to reliable cyclic voltammetry measurements for the determination of double layer capacitance[J]. J. Phys.: Energy, 2021, 3(3): 034013.
[31] Nishihara Y, Nakajima Y, Akashi A, Tsujino N, Takahashi E, Funakoshi K I, Higo Y. Isothermal compression of face-centered cubic iron[J]. Am. Mineral., 2012, 97(8−9): 1417−1420.
[32] Sevilla M, Antonio B F. Catalytic graphitization of templated mesoporous carbons[J]. Carbon, 2006, 44(3): 468−474.
[33] Yu H Y, Fisher A, Cheng D J, Cao D P. Cu, N-codoped hierarchical porous carbons as electrocatalysts for oxygen reduction reaction[J]. ACS Appl. Mater. Interfaces, 2016, 8(33): 21431−21439.
[34] Liu M C, Guo X H, Hu L B, Yuan H F, Wang G, Dai B, Zhang L L, Yu F. Fe_3O_4/Fe_3C@ nitrogen-doped carbon for enhancing oxygen reduction reaction[J]. ChemNanoMat, 2019, 5(2): 187−193.
[35] Yan C C, Li H B, Ye Y F, Wu H H, Cai F, Si R, Xiao J P, Miao S, Xie S H, Yang F, Li Y S, Wang G X, Bao X H. Coordinatively unsaturated nickel-nitrogen sites towards selective and high-rate CO_2 electroreduction[J]. Energy Environ. Sci., 2018, 11(5): 1204−1210.
[36] Li B, Sasikala S P, Kim D H, Bak J, Kim D, Cho E A, Kim S O. Fe-N_4 complex embedded free-standing carbon fabric catalysts for higher performance ORR both in alkaline & acidic media[J]. Nano energy, 2019, 56: 524−530.
[37] Peng X M, Wu J Q, Zhao Z L, Wang X, Dai H L, Li Y M, Wei Y, Xu G P, Hu F P. High efficiency degradation of tetracycline by peroxymonosulfate activated with Fe/NC catalysts: performance, intermediates, stability and mechanism[J]. Environ. Res., 2022, 205: 112538.
[38] Guo J H, Zhang S, Zheng M, Tang J, Liu L, Chen J M, Wang X C. Graphitic-N-rich N-doped graphene as a high performance catalyst for oxygen reduction reaction in alkaline solution[J]. Int. J. Hydrogen Energy, 2020, 45(56): 32402−32412.
[39] Li X G, Ni L, Zhou J H, Xu L, Lu C L, Yang G X, Ding W P, Hou W H. Encapsulation of Fe nanoparticles into an N-doped carbon nanotube/nanosheet integrated hierarchical architecture as an efficient and ultrastable electrocatalyst for the oxygen reduction reaction[J]. Nanoscale, 2020, 12(26): 13987−13995.
[40] Liu D, Srinivas K, Chen X, Ma F, Zhang X J, Wang X Q, Wang B, Chen Y F. Dual Fe, Zn single atoms anchored on carbon nanotubes inlaid N, S-doped hollow carbon polyhedrons for boosting oxygen reduction reaction[J]. J Colloid Inter. Sci., 2022, 624: 680−690.
[41] Wang N N, Li J, Hei J P, Chen X D, Yin X J, Cai C W, Li M L, Cui L F. ε-Fe_3N@N-doped carbon core-shell nanoparticles encapsulated in bamboo-like carbon nanotubes for oxygen reduction reaction[J]. Mater. Chem. Phys., 2022, 291: 126769.
[42] Talukder N, Wang Y, Nunna B B, Lee E S. An in-depth exploration of the electrochemical oxygen reduction reaction (ORR) phenomenon on carbon-based catalysts in alkaline and acidic mediums[J]. Catalysts, 2022, 12(7): 21.
[43] Li X, Ni L, Zhou J H, Xu L, Lu C N, Yang G X, Ding W P, Hou W H. Encapsulation of Fe nanoparticles into an N-doped carbon nanotube/nanosheet integrated hierarchical architecture as an efficient and ultrastable electrocatalyst for the oxygen reduction reaction[J]. Nanoscale, 2020, 12(26): 13987−13995.
[44] Park S, Her M, Shin H J, Hwang W, Sung Y E. Maximizing the active site densities of single-atomic Fe-N-C electrocatalysts for high-performance anion membrane fuel cells [J]. ACS Appl. Energy Mater., 2021, 4: 1459−1466.
[45] Freitas W DS, Pico M PP, DEpifanio A, Mecheri B. Nanostructured Fe-N-C as bifunctional catalysts for oxygen reduction and hydrogen evolution[J]. Catalysts, 2021, 11: 1525.

[46] Gao J, Ma N, Zheng Y M, Zheng J F, Gui J Z, Guo C K, An H Q, Yin Z, Ma D. Cobalt/nitrogen-doped porous carbon nanosheets derived from polymerizable ionic liquids as bifunctional electrocatalyst for oxygen evolution and oxygen reduction reaction[J]. ChemCatChem, 2017, 9(9): 1601−1609.

[47] Yuan K, Lutzenkirchen-Hecht D, Li L B, Shuai L, Li Y Z, Cao R, Qiu M, Zhuang X D, Leung M KH, Chen Y W, Scherf U. Boosting oxygen reduction of single iron active sites via geometric and electronic engineering: nitrogen and phosphorus dual coordination[J]. J. Am. Chem. Soc., 2020, 142: 2404−2412.

[48] Zhang X B, Han X, Jiang Z, Xu J, Chen L N, Xue Y K, Nie A, Xie Z X, Kuang Q, Zheng L S. Atomically dispersed hierarchically ordered porous Fe-N-C electrocatalyst for high performance electrocatalytic oxygen reduction in Zn-air battery[J]. Nano Energy, 2020, 71: 104547.

[49] Ye Y F, Li H B, Cai F, Yan C C, Si R, Miao S, Li Y S, Wang G X, Bao X H. Two-dimensional mesoporous carbon doped with Fe-N active sites for efficient oxygen reduction [J]. ACS Catal, 2017, 7: 7638−7646.

[50] Jiao L, Wan G, Zhang R, Zhou H, Yu S H, Jiang H L. From metal-organic frameworks to single-atom Fe implanted N-doped porous carbons: efficient oxygen reduction in both alkaline and acidic media[J]. Angew. Chem. Int. Ed., 2018, 57: 8525−8529.

[51] Li G N, Zhang J J, Li W S, Fan K, Xu C J. 3D interconnected hierarchical porous N-doped carbon constructed by flake-like nanostructure with Fe/Fe_3C for efficient oxygen reduction reaction and supercapacitor[J]. Nanoscale, 2018, 10(19): 9252−9260.

[52] Mahmood J, Li F, Kim C, Choi H J, Gwon O, Jung S M, Seo J M, Cho S J, Ju Y W, Jeong H Y, Kim G. Fe@C_2N: a highly-efficient indirect-contact oxygen reduction catalyst [J]. Nano Energy, 2018, 44: 304−310.

[53] Liu S, Li C, Zachman M J, Zeng Y C, Yu H R, Li B Y, Wang M Y, Braaten J, Liu J W, Meyer III H M, Lucero M, Kropf A P, Alp E E, Gong Q, Shi Q R, Feng Z X, Xu H, Wang G F, Myers D J, Xie J, Cullen D A, Litster S, Wu Gang. Atomically dispersed iron sites with a nitrogen-carbon coating as highly active and durable oxygen reduction catalysts for fuel cells[J]. Nat. Energy, 2022, 7(7): 652−663.

[54] Park H S, Han S B, Kwak D H, Han J H, Park K W. Fe nanoparticles encapsulated in doped graphitic shells as high-performance and stable catalysts for oxygen reduction reaction in an acid medium[J]. J. Catal., 2019, 370: 130−137.

[55] Jiang X L, Yang Y Y, Zhu C L, Zhang R, Wu F, Wu H H, Wang J. Atomically dispersed Fe-Nx sites doped mesopore-dominated carbon nanodisks towards efficient oxygen reduction[J]. Int. J. Hydrogen Energy, 2022, 47(78): 33308−33318.

[56] Wang Y, Chen Y, Wang Z W, Li P, Zhao J Y, Zhao H Y, Li D, He T X, Wei Y T, Su Y Q, Xiao C H. Boron doping induced electronic reconfiguration of Fe-Nx sites in N-doped carbon matrix for efficient oxygen reduction reaction in both alkaline and acidic media[J]. Int. J. Hydrogen Energy, 2022, 47(43): 18663−18674.

[57] Bai J, Ge W, Zhou P, Xu P, Wang L, Zhang J, Jiang X, Li X, Zhou Q. Precise constructed atomically dispersed Fe/Ni sites on porous nitrogen-doped carbon for oxygen reduction[J]. J. Colloid Inter. Sci., 2022, 616: 433−439.

[58] Gao J, Hu Y, Wang Y, Lin X, Hu K, Lin X, Xie G, Liu X, Reddy K M, Yuan Q, Qiu H J. MOF structure engineering to synthesize Co-N-C catalyst with richer accessible active sites for enhanced oxygen reduction[J]. Small, 2021, 17(49): e2104684.

[59] Cui L F, Chen M X, Huo G, Fu X Z, Luo J G. FeCo nanoparticles wrapped in N-doped carbon derived from Prussian blue analogue and dicyandiamide as efficient oxygen reduction electrocatalysts for Al-air batteries[J]. Chem. Eng. J., 2020, 395: 125158.

[60] Li W J, Wang F, Zhang Z G, Min S X. Graphitic carbon layer-encapsulated Co nanoparticles embedded on porous carbonized wood as a self-supported chainmail oxygen electrode for rechargeable Zn-air batteries[J]. Appl. Catal. B, 2022, 317: 121758.

[61] Liu Z F, Ye D D, Zhu X, Wang S L, Zou Y N, Lan L H, Chen R, Yang Y, Liao Q. ZIF-67-derived Co nanoparticles embedded in N-doped porous carbon composite interconnected by MWCNTs as highly efficient ORR electrocatalysts for a flexible direct formate fuel cell[J]. Chem. Eng. J., 2022, 432: 134192.

氮掺杂多孔碳包覆铁纳米粒子催化剂用于高效碱性介质中氧还原反应

李春艳，张　蕊，巴笑杰，姜晓乐*，阳耀月*
化学基础国家民委重点实验室，西南民族大学化学与环境学院，四川 成都 610041

摘要

合理设计和合成非贵金属催化剂对提高氧还原反应的催化活性和稳定性具有重要意义，但仍然存在重大挑战。本工作采用功能化金属有机框架材料为前驱体，合成了氮掺杂多孔碳包覆 Fe 纳米粒子催化剂（Fe@N-C）。Fe 纳米颗粒的嵌入提高了催化剂的石墨化程度和石墨化氮的比例，同时促进了中孔的形成。Fe@N-C-30 催化剂在碱性溶液中表现出良好的氧还原反应活性（E_0 = 0.97 V vs. RHE，$E_{1/2}$ = 0.89 V vs. RHE）。此外，与商用 Pt/C 相比，Fe@N-C-30 催化剂具有更好的耐甲醇性和循环稳定性。其优异的电催化活性归因于高的电化学表面积、相对高比例的石墨化氮、独特的孔结构以及包覆的 Fe 颗粒与碳层之间的协同效应。本工作为利用金属有机框架材料制备高效非贵金属 ORR 催化剂提供了一种有前景的方法。

关键词：金属有机框架；多孔结构；铁纳米粒子；氧还原反应